

## Optical boundary reconstruction of tokamak plasmas for feedback control of plasma position and shape

G. Hommen,<sup>1,2</sup> M. de Baar,<sup>1,2</sup> P. Nuij,<sup>1</sup> G. McArdle,<sup>3</sup> R. Akers,<sup>3</sup> and M. Steinbuch<sup>1</sup>

<sup>1</sup>*Control Systems Technology Group, Eindhoven University of Technology, P.O. Box 513, 5600 MB Eindhoven, The Netherlands*

<sup>2</sup>*FOM Institute for Plasma Physics "Rijnhuizen," Association EURATOM-FOM, Trilateral Euregio Cluster, P.O. Box 1207, 3430 BE Nieuwegein, The Netherlands*

<sup>3</sup>*EURATOM/CCFE Fusion Association, Culham Science Centre, Abingdon, Oxfordshire OX14 3DB, United Kingdom*

(Received 22 June 2010; accepted 13 September 2010; published online 10 November 2010)

A new diagnostic is developed to reconstruct the plasma boundary using visible wavelength images. Exploiting the plasma's edge localized and toroidally symmetric emission profile, a new coordinate transform is presented to reconstruct the plasma boundary from a poloidal view image. The plasma boundary reconstruction is implemented in MATLAB and applied to camera images of Mega-Ampere Spherical Tokamak discharges. The optically reconstructed plasma boundaries are compared to magnetic reconstructions from the offline reconstruction code EFIT, showing very good qualitative and quantitative agreement. Average errors are within 2 cm and correlation is high. In the current software implementation, plasma boundary reconstruction from a single image takes 3 ms. The applicability and system requirements of the new optical boundary reconstruction, called OFIT, for use in both feedback control of plasma position and shape and in offline reconstruction tools are discussed. © 2010 American Institute of Physics. [doi:10.1063/1.3499219]

### I. MEASUREMENT AND CONTROL OF TOKAMAK PLASMA POSITION AND SHAPE

Reconstruction of the tokamak plasma boundary is used for both real-time control applications and offline analysis tools. Control of plasma position and shape in tokamaks is used to optimize plasma performance, access specific physics regimes, and protect first-wall components.<sup>1-4</sup> Offline reconstruction tools such as EFIT (Ref. 5) are used for postdischarge analysis using a wide range of diagnostics and would greatly benefit from the determination of an accurate plasma boundary.

In present day tokamaks, magnetic measurements from a set of coils located around the vacuum vessel are used to measure flux variations. After integration, the fluxes are interpreted in terms of the plasma centroid position and velocity, the plasma boundary as defined by the last closed flux surface (LCFS), and the location of the x-point(s) and the strike points. The full magnetic topology of flux surfaces cannot be determined in detail without the use of additional, internal diagnostics such as polarimetry or the motional Stark effect.<sup>6</sup> Simultaneous control of the current and pressure profile in tokamaks relies on the real-time identification of the full magnetic topology, the reconstruction of which would greatly benefit from an unambiguous plasma boundary.

There are a number of limitations to magnetic boundary reconstruction. Firstly, the integration of the time derivative of the fluxes can lead to drifts in the flux measurements on time-scales that are relevant for a reactor.<sup>7</sup> The reconstruction of the flux surfaces must take into account the passive conducting structures of the tokamak. Often these structures,

such as the iron core in the Joint European Torus, exhibit nonlinear behavior which hampers the interpretation of magnetic signals.<sup>8</sup> During startup or in optimized shear discharges, the flux distribution is far from equilibrium and there are strong transients. The reconstruction of the plasma boundary using only external magnetic measurements is problematic in such dynamic situations. Diagnostics coils measuring poloidal fields are very sensitive to alignment; small misalignments can cause large disturbances from the much stronger toroidal field.

To address these problems, an alternative plasma boundary diagnostic is developed using high speed camera images of the visible light emitted by the plasma edge. The camera data do not suffer from drift, are intrinsically robust against the aforementioned transients, and provide an independent measurement of the optical plasma boundary. The exact relation between optical plasma boundary and the magnetic plasma boundary, however, remains to be investigated. The captured images provide information not only on the plasma boundary but also show filament structures, edge localized modes (ELMs),<sup>9</sup> distinct confinement regimes such as L-mode and H-mode, and hot spots on plasma-facing components (PFCs). The diagnostic could be extended to provide information on these plasma edge specific phenomena with high accuracy relative to the plasma edge and create an opportunity for intelligent, integrated sensing and control of not only the plasma position and shape, but also the resulting heat-fluxes to plasma-facing components. A previous work on optical plasma boundary reconstruction<sup>10</sup> for offline applications has already shown promising results, although the applied reconstruction was only valid on the equatorial mid-plane and produced significant errors elsewhere.

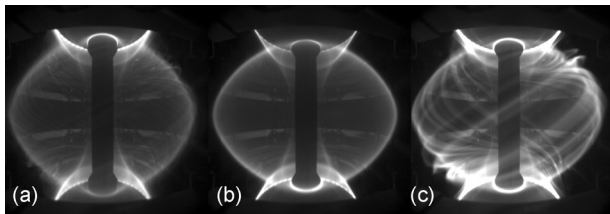


FIG. 1. Images of MAST shot no. 23344, showing (a) L-mode, (b) H-mode, and (c) ELM plasmas, respectively.

This paper introduces an optical plasma boundary reconstruction and, using camera images from the Mega-Ampere Spherical Tokamak (MAST),<sup>11</sup> compares the obtained shape of the radiative shell to EFIT reconstructions of the magnetic plasma boundary. The feasibility of the developed plasma boundary diagnostic for use in a feedback control loop on MAST is assessed, as well as possible applications in offline analysis tools.

The paper is organized as follows. A new coordinate transform for the reconstruction of the plasma boundary from a poloidal view image is presented and synthetic reconstructions are shown to illustrate the properties of this transform in Sec. II. A MATLAB implementation of the new diagnostic is then applied to poloidal view images of MAST discharges and the resulting plasma boundaries are compared to magnetic reconstructions from EFIT in Sec. III. Section IV discusses the usability of the new diagnostic in feedback control systems of plasma position and shape and highlights a number of applications in offline analysis tools. The main results are summarized in Sec. V.

## II. PLASMA BOUNDARY RECONSTRUCTION USING TWO-DIMENSIONAL-VISIBLE IMAGING

Figure 1 shows camera images of MAST plasmas in which the plasma edge is clearly visible. As only the plasma edge emits a significant amount of light from a thin shell, for the purpose of real-time plasma boundary reconstruction, the plasma edge is treated as a thin, toroidally symmetric emissive surface  $S_p$  that is the boundary of the plasma volume  $\Omega_p$ .

Every pixel of an image is a line integrated measurement of the light emitted by the plasma. Pixels corresponding to a line of sight that is tangent to the emissive surface  $S_p$  will show a peak in intensity compared to neighboring sightlines that either cross the plasma surface or miss it altogether.

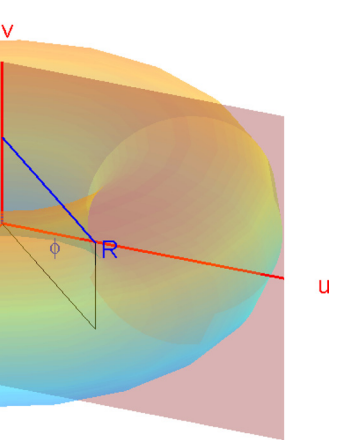
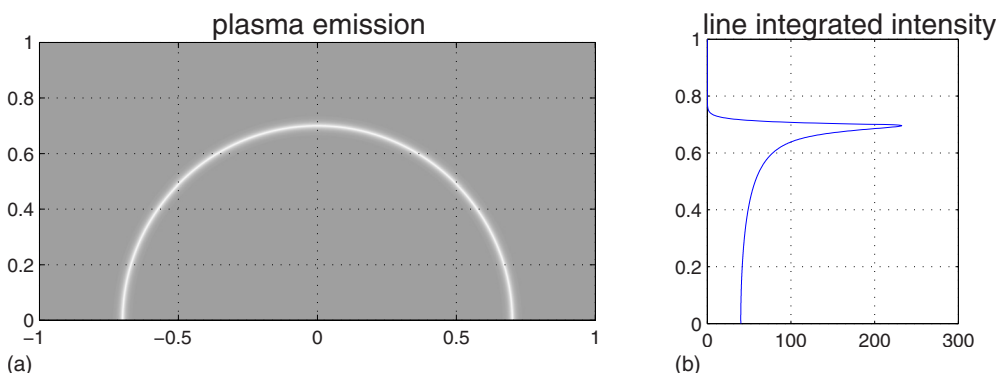


FIG. 3. (Color online) Cartesian and tokamak coordinates, a circular plasma, and the projection surface on the  $(u,v)$  plane.

Figure 2 shows the plasma emission in the tokamak mid-plane  $(u,w)$  and the resulting pixel intensities for horizontal sightlines. The plasma edge in image can now be identified as lines of peak intensity, corresponding to the set of pixels  $p_e$  that have a line of sight  $l_e$  tangent to the plasma surface  $S_p$ .

### A. Coordinate transform: From image to tokamak coordinates

For the plasma shape reconstruction, a new coordinate transform is derived to reconstruct the toroidally symmetric plasma surface  $S_p$  from the set of sightlines  $l_e$  from a single camera tangent to the plasma surface  $S_p$ . The problem is defined in two coordinate systems, a Cartesian system  $(u,v,w)$  and the cylindrical tokamak coordinate system  $(R,Z,\phi)$ , where the origin and the  $v$  and  $Z$  axes of both coordinate systems coincide and the point  $(0,0,\phi)$  in tokamak coordinates is the center of the tokamak. A projection plane is defined as the vertical  $(u,v,0)$  plane. Figure 3 shows the two coordinate systems and the projection plane. Given the camera location  $(u_c, v_c, w_c)$  and knowledge of the projection properties of the optics, the trajectories of all sightlines  $l$  are known and each has a projection  $(u,v)$  on the projection plane. In the ideal case of a perfect pinhole camera with its optical axis normal to the projection surface, the projection  $(u,v)$  of sightlines on the projection surface is an affine scaling of the pixel coordinates  $(x,y)$ . Any type of projection can

FIG. 2. (Color online) (a) Emission profile of the plasma in the equatorial plane and (b) resulting line integrated intensity for horizontal sightlines parallel to the  $w$ -axis.

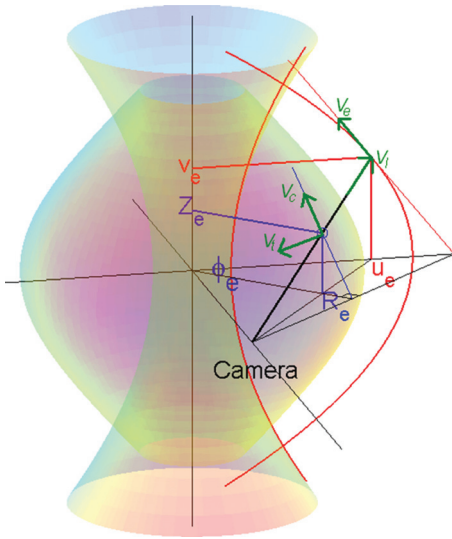


FIG. 4. (Color) Perspective view of lines on projection plane (red), sightline  $l_e$  (thick black line), tokamak coordinates  $R$  and  $Z$  (blue lines), and tangent point on plasma surface (blue circle). Also shown are the vectors used in the coordinate transform in green.

be accounted for with a suitable projection function.  $(u, v) = f(x, y)$ .

The sightline  $l_e$  of an edge pixel  $p_e$  is tangent to the plasma surface but the point of tangency along the sightline is not directly known. To find this point, the tangency is expressed as a vector equation. The vectors introduced hereafter are drawn in Fig. 4. Figure 5 also depicts the coordinate transform, but in this image the projection plane is shifted backward  $(u, v, -1.5)$  for another look at the situation. The projection plane can be moved along the  $w$  axis arbitrarily, however, choosing  $(u, v, 0)$  provides the mathematically simplest solution.

The plasma surface is known to be toroidally symmetric, such that at each point  $(R, Z, \varphi)$  on  $S_p$  the surface is spanned

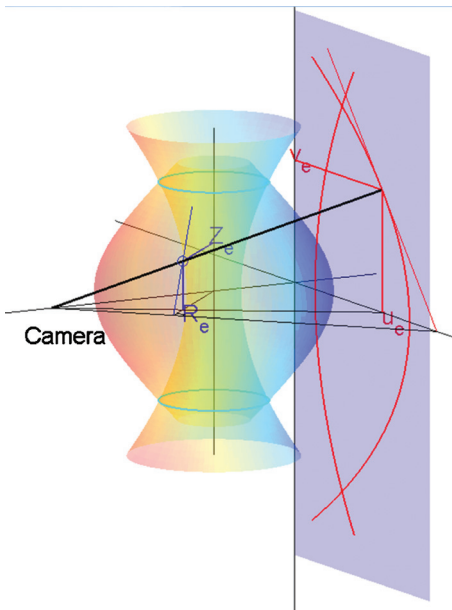


FIG. 5. (Color) Similar to Fig. 4 but with the projection plane shifted backward for clarity.

by two vectors in Cartesian coordinates  $(u, v, w)$

$$V_t = \begin{bmatrix} -\sin(\varphi) \\ 0 \\ \cos(\varphi) \end{bmatrix}, \quad V_c = \begin{bmatrix} \frac{dR}{dZ} \cos(\varphi) \\ 1 \\ \frac{dR}{dZ} \sin(\varphi) \end{bmatrix},$$

being the toroidal unit vector and the local conicity. Additionally, the sightline vector of  $l_e$  is

$$V_l = \begin{bmatrix} u_e - u_c \\ v_e - v_c \\ -w_c \end{bmatrix},$$

where  $(u_e, v_e)$  is the projection of  $l_e$  on the projection surface. This set of vectors does not uniquely specify the tangent point along a sightline, as  $R$  and  $Z$  are unknown and  $V_l$  and  $V_t$  are not multiples. To obtain an additional vector, the set of tangent sightlines is treated as a curved sight surface. Locally, this surface is spanned by the sightline  $l_e$  and the direction of the plasma edge on the projection plane at  $(u_e, v_e)$ . This allows introduction of the edge vector  $V_e$  as the direction along the plasma edge in the projection plane

$$V_e = \begin{bmatrix} \frac{du_e}{dv_e} \\ 1 \\ 0 \end{bmatrix},$$

such that the sightsurface along a sightline is spanned by  $V_l$  and  $V_e$ . The toroidal angle  $\varphi_e$  of the tangent point on the sightline can now be obtained from the vector equation

$$V_t = \begin{bmatrix} -\sin(\varphi_e) \\ 0 \\ \cos(\varphi_e) \end{bmatrix} = \alpha V_l + \beta V_e = \alpha \begin{bmatrix} u_e - u_c \\ v_e - v_c \\ -w_c \end{bmatrix} + \beta \begin{bmatrix} \frac{du_e}{dv_e} \\ 1 \\ 0 \end{bmatrix}. \tag{1}$$

By substitution of  $\alpha$  and  $\beta$ , this leads to

$$\tan(\varphi_e) = \frac{(u_e - u_c) - \frac{du_e}{dv_e}(v_e - v_c)}{w_c}. \tag{2}$$

Given the sightline  $l_e$  and the toroidal angle  $\varphi_e$  of the tangent point,  $(R_e, Z_e, \varphi_e)$  can be found as well as the conicity  $dR_e/dZ_e$  of the plasma surface at  $(R_e, Z_e, \varphi_e)$ . In Fig. 4, a perspective view of the plasma surface and the projection plane shows how the points  $R_e$  and  $Z_e$  are defined by  $l_e$  and  $\varphi_e$ .

Expressing  $R_e$  and  $Z_e$  in terms of  $u_e, v_e$ , and  $\varphi_e$

$$R_e = \frac{u_e w_c}{w_c \cos \varphi_e + (u_e - u_c) \sin \varphi_e}, \tag{3}$$

$$Z_e = v_c + (v_e - v_c) \frac{(w_c - R_e \sin \varphi_e)}{w_c}, \tag{4}$$

completes the coordinate transform. Important to note is the derivative term  $du_e/dv_e$  in Eq. (2). This term must be deter-

mined either as a numerical derivative between edge points  $p_e$  or as the derivative of a smooth function fitted to the edge points.

Given the set of tangent sightlines  $l_e$ , a reconstruction of the toroidally symmetric plasma surface  $S_p$  can now be made. The result is generally presented as a poloidal cross section of the plasma surface.

### 1. Deviations from toroidal symmetry: Ripple

The assumption of toroidal symmetry of the plasma surface may not hold exactly; in tokamaks with a significant toroidal field ripple, caused by the limited number of toroidal field coils, the plasma boundary may be somewhat deformed.

It is assumed that a ripple in toroidal field results in a periodic disturbance of the major radius of the (outer) flux surfaces of the form

$$R = R_0 + \Delta R(R_0, Z) \sin(N\varphi). \quad (5)$$

Depending on the magnitude and frequency of the ripple, three distinct regimes can be identified. When the periodic deformation of the plasma boundary is small, in the order of the thickness of the emissive layer, and the frequency of the ripple is high, for example, more than ten periods per rotation, ripple is expected to broaden the edge in the image of the plasma. This will result in a lower accuracy of the plasma boundary reconstruction.

When the deformation of the plasma boundary is much bigger than the thickness of the emissive layer, multiple plasma edges can show up in the image. This regime is, however, not observed in any tokamak, but can be seen in stellarators, which are strongly nonaxisymmetric. In this case the toroidal surface reconstruction cannot be applied.

Limited deviations from toroidal symmetry with limited spatial frequency can result in small displacements of the plasma edge in the image when compared to the toroidally symmetric case. This regime can be handled by the coordinate transform. A toroidally symmetric plasma surface is spanned at any point by two vectors: the toroidal unit vector  $V_t$  and the local conicity  $V_c$ , as introduced earlier. A rippled plasma surface, however, will have a different orientation in the horizontal plane and is not spanned by the toroidal unit vector  $V_t$ . To define the horizontal orientation of a rippled plasma surface, the angle  $\alpha$  is introduced and the toroidal unit vector is replaced by the ripple vector  $V_{\text{ripple}}$

$$V_{\text{ripple}} = \begin{bmatrix} -\sin(\alpha) \\ 0 \\ \cos(\alpha) \end{bmatrix},$$

where  $\alpha$  is the angle between the ripple vector  $V_{\text{ripple}}$  and the  $w$ -axis. Applying  $V_{\text{ripple}}$  in Eqs. (1) and (2), Eq. (2) now provides the horizontal orientation of the plasma surface at the point of tangency. Using the knowledge of the rippled toroidal field, the horizontal orientation of the plasma surface  $\alpha$  can be determined at any point  $(R, Z, \varphi)$  and thus also along a sightline. Figure 6 shows the angle  $\alpha$  along a mid-plane sightline for an arbitrary rippled plasma of the form

$$\alpha = \varphi + f_{\text{ripple}} R^2 \sin(N\varphi). \quad (6)$$

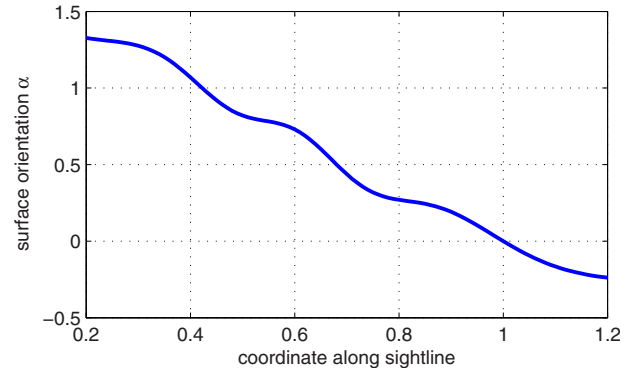


FIG. 6. (Color online) Horizontal surface orientation along sightline.

As Eq. (2) determines the horizontal orientation of the plasma surface at the point of tangency, the point of tangency on the sightline can now be found by matching the result of Eq. (2) to the point on the sightline with the same orientation  $\alpha$ . Once this point is found, the rippled major radius  $R$  can be mapped back to the nominal radius  $R_0$  using the angle  $\varphi$  of the tangent point.

A prerequisite is that  $\alpha$  is monotonically increasing or decreasing along the sightline. This limits the maximum magnitude and spatial frequency of ripple that can be handled by the toroidal surface reconstruction.

### B. Inverse coordinate transform: From tokamak to image coordinates

The inverse toroidal surface reconstruction allows to construct the projection of the plasma edges on the projection plane  $(u, v, 0)$  for a given plasma boundary and camera location. The approach is the same as for the transform from projection plane to plasma surface. At the point  $(R, Z, \varphi)$ , the plasma surface  $S_p$  is spanned by the toroidal unit vector and the conicity  $dR/dZ$  of the surface

$$V_t = \begin{bmatrix} -\sin(\varphi) \\ 0 \\ \cos(\varphi) \end{bmatrix}, \quad V_c = \begin{bmatrix} \frac{dR_e}{dZ_e} \cos(\varphi) \\ 1 \\ \frac{dR_e}{dZ_e} \sin(\varphi) \end{bmatrix}.$$

For a given camera location  $(u_c, v_c, w_c)$ , the sightline tangent to  $(R_e, Z_e, \varphi)$  is sought. The direction of this sightline is expressed as the vector

$$V_l = \begin{bmatrix} u_e - u_c \\ v_e - v_c \\ -w_c \end{bmatrix}.$$

Using Eqs. (3) and (4),  $u_e - u_c$  and  $v_e - v_c$  can be expressed in terms of  $R_e$ ,  $Z_e$ ,  $\varphi_e$ ,  $u_c$ ,  $v_c$ , and  $w_c$ ,

$$u_e - u_c = w_c \frac{R_e \cos(\varphi_e) - u_c}{w_c - R_e \sin(\varphi_e)}, \quad (7)$$

$$v_e - v_c = w_c \frac{Z_e - v_c}{w_c - R_e \sin(\varphi_e)}, \quad (8)$$

in which  $u_e$ ,  $v_e$ , and  $\varphi_e$  are unknown. Now, the sightline vector  $V_l$  can be spanned by  $V_t$  and  $V_c$

$$V_l = \chi V_t + \delta V_c, \quad (9)$$

which, after rewriting, results in the expression used to find  $\varphi_e$

$$u_c \cos(\varphi_e) + w_c \sin(\varphi_e) = R_e - (Z_e - v_c) \frac{dR_e}{dZ_e},$$

which can be further simplified to

$$\sqrt{u_c^2 + w_c^2} \sin \left[ \varphi_e + \arctan \left( \frac{u_c}{w_c} \right) \right] = R_e - (Z_e - v_c) \frac{dR_e}{dZ_e}, \quad (10)$$

such that Eqs. (7)–(10) form the complete inverse transform.

The inverse coordinate transform can be used to derive the limits of the plasma dimensions that can be reconstructed from the image given the limits of view in the projection plane and the location of the camera. The expression for the toroidal angle  $\varphi_e$  of the tangent point on a sightline tangent to the plasma surface at  $(R, Z)$ , Eq. (10), has a solution only when

$$\sqrt{u_c^2 + w_c^2} \geq \left| R_e - (Z_e - v_c) \frac{dR_e}{dZ_e} \right|, \quad (11)$$

implying that the camera must be located *outside* a cone that fits around the plasma surface at  $(R_e, Z_e, dR_e/dZ_e)$  to be able to see this part of the plasma surface. Also taking into account the limited viewing angle of the camera, the projection points  $(u_e, v_e)$  obtained from the inverse transform must lie inside the area of the projection plane viewed by the camera. The existence of the transform, i.e., the visibility in the camera image of the plasma edge at  $(R_e, Z_e, dR_e/dZ_e)$ , thus depends on the camera location and the maximum viewing angle of the optics. This knowledge can be helpful in determining the optimum camera location for an optical plasma boundary diagnostic.

For the special case of a circular plasma cross section, the newly derived coordinate transform is mathematically validated in Appendix A.

### C. Example of shape reconstruction from an image and image synthesis from a plasma shape

To illustrate the mechanism of the derived coordinate transform, two examples are treated: the synthesis of a camera image showing a circular plasma and the plasma shape reconstruction from a double null diverter (DND) plasma image.

For the image synthesis, a circular plasma cross section with a major radius  $R_0 = 2.25$  m and a minor radius  $r = 0.4$  m is used, similar to plasmas generated in the Tore Supra tokamak<sup>12</sup> with reduced minor radius. The camera location is chosen to be  $(u_c, v_c, w_c) = (-2, -0.3, 2.5)$ ; a location that provides a poloidal view from 30 cm below equatorial height, viewing the plasma around toroidal angle  $\varphi = -\pi$ .

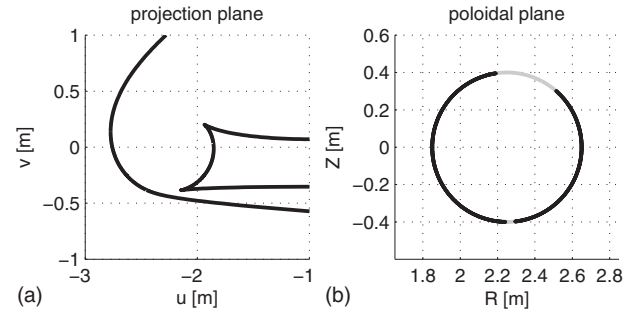


FIG. 7. (a) Projection of circular plasma with minor radius  $r=0.4$ . (b) Plasma circumference, gray where no projection exists for the applied camera position.

The plasma shape in the poloidal plane  $(R, Z)$  can now be expressed in terms of the poloidal angle  $\theta$

$$R_e = R_0 + r \cos(\theta),$$

$$Z_e = r \sin(\theta), \quad (12)$$

which allows writing  $dR/dZ$  as

$$\frac{dR_e}{dZ_e} = \frac{dR_e}{d\theta} \left( \frac{dZ_e}{d\theta} \right)^{-1} = \frac{-r \sin(\theta)}{r \cos(\theta)} = -\tan(\theta). \quad (13)$$

Using this description of the plasma edge and applying the transform derived in Sec. II B results in the projection of the plasma edge on the projection plane. In this case, the projection plane is treated directly as the image, effectively taking the camera projection properties out of the problem. Figure 7(a) shows the resulting plasma edges in the projection plane.

The plasma edge in the projection plane is not a circle. Instead, the inner and outer halves of the plasma circumference result in two separate curves. For the top and bottom of the circular plasma shape,  $\theta \sim \pi/2$  and  $\theta \sim 3\pi/2$ , the condition of Eq. (11) is not met for the given camera location and no projection exists. More generally, Eq. (11) shows any horizontal part of the plasma circumference, where  $(dR_e/dZ_e)^{-1} = 0$  is only visible when  $Z_e = v_c$ . In practice, the top and bottom of a circular plasma circumference therefore typically do not appear in the image.

The projection of the inner plasma edge in Fig. 7(a) is discontinuous, the projection around the midplane is approximately circular while the top, and bottom of the plasma appear as two tails stretching out around the torus. This effect also appears in camera images of circular plasmas such as the Tore Supra camera image shown in Fig. 8. In Fig. 9,



FIG. 8. (Color online) Image of detached circular plasma in Tore Supra.

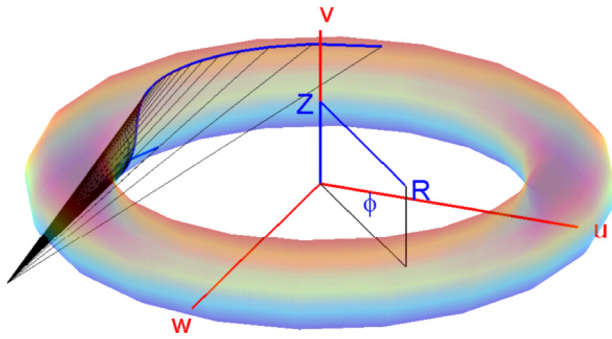


FIG. 9. (Color online) Tangent sightlines around the inner edge of a circular cross section plasma in Tore Supra geometry.

the sightlines tangent to the inner plasma surface are drawn. Around the equatorial plane, the toroidal angle of tangency  $\varphi_e$  is approximately constant, resulting in a projection that is circular. The strong rise in  $\varphi_e$  near the top and bottom of the plasma surface, however, results in projection from points around the back half of the torus. The top and bottom of the plasma surface are near-horizontal and are at a large horizontal distance from the camera, meaning the term  $(Z-v_c)dR/dZ$  in Eq. (8) is large and, as a result,  $\varphi_e$  will be large.

For the shape reconstruction of the DND plasma from a camera image, the projected plasma edges are presented as two curves on the  $(u, v, 0)$  projection plane as shown in Fig. 10(a). The camera dependent projection from pixel coordinates to projection surface is not regarded. For simplicity, the projected plasma edges are described by two second order polynomials of the form

$$u = a_0 + a_2 v^2, \quad (14)$$

such that

$$\frac{du}{dv} = 2a_2 v. \quad (15)$$

The coefficients of the inner and outer edge are chosen such that the two lines cross at  $v = \pm 1.4$  m and DND plasma

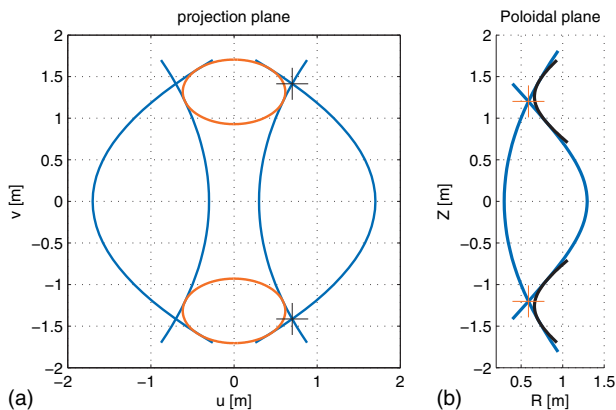


FIG. 10. (Color) (a) Projection plane, showing the image of plasma edge, x-point (red circles), and intersection of edges (black cross). (b) Poloidal cross section, showing the plasma shape, x-points (red crosses), and projection of sightlines corresponding to the intersection of edges in the projection plane (black lines).

image is obtained. Applying the coordinate transform presented in Sec. II A to these curves results in the poloidal plasma cross section as shown in Fig. 10(b).

The coordinate transform results in different deformations of the resulting inner and outer plasma edges because of the opposite signs of the  $du/dv$  terms. While both curves in the projection plane are defined in the region  $-1.7 < v < 1.7$ , a different region is spanned in the  $Z$  coordinate.

The transform of two points at  $(u_e, v_e)$  with different values of  $du/dv$  results in two different points  $(R_e, Z_e)$  in the poloidal plane. The intersections of the curves in the projection plane therefore do not correspond to the intersections of the curves in the poloidal plane, implying that the crossing of the plasma edges in a camera image does not relate to the plasma x-point! The sightline corresponding to the intersection point on the projection plane is tangent to both the inner and the outer plasma surface but at different distances from the camera, thus at different points  $(R_e, Z_e)$ . To illustrate this, the trajectory of this sightline in the poloidal plane is drawn in black in Fig. 10(b). This results in a curve that is tangent to the inner and the outer plasma edge, but at different points.

The optically reconstructed x-points are shown as the red crosses in Fig. 10(b). A point in the poloidal cross section  $(R, Z)$  corresponds to a circle in tokamak coordinates  $(R, Z, \varphi)$ . The projections of these x-point circles are drawn in the projection plane, shown in red in Fig. 10(a). The resulting circles are tangent to both plasma edges in the projection plane. Concluding, tokamak plasma x-points are not directly visible in an image of the plasma but their location can be derived from the reconstructed plasma surfaces in the poloidal plane.

When drawing the trajectory of the tangent sightlines  $l_e$  in the poloidal plane, horizontal sightlines have a straight, horizontal trajectory, while vertically inclined sightlines show a parabola trajectory. These trajectories can be treated as upper bounds on the  $R$  coordinate of the plasma edge. Nearly horizontal sightlines are therefore desired for optimum resolving power, as they impose only a very local upper bound on  $R$ . Figure 11 shows the top half of the DND plasma shape in the poloidal cross section with the trajectories of the tangent sightlines used to reconstruct the plasma shape. The resolving power of the reconstruction is highest around the equatorial plane, where sightlines are nearly horizontal.

### III. EXPERIMENTAL RESULTS ON MAST

To test the optical plasma boundary reconstruction, or OFIT, camera images from MAST discharges providing a full view of the plasma are used. The optical reconstruction procedure is described and the results are compared to plasma boundaries derived from magnetic measurements by the EFIT (Ref. 5) code. As the two forms of boundary reconstruction are based on different physical properties of the plasma, an exact agreement is not to be expected. The comparison of the two reconstructions may indicate a possible relation between the magnetic and emissive properties of the plasma edge.

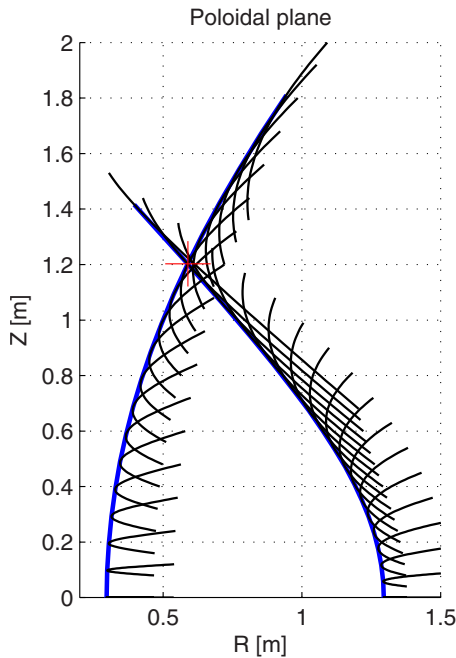


FIG. 11. (Color online) Top half of plasma shape in poloidal plane, showing projections of tangent sightlines used to reconstruct the plasma shape.

### A. Camera calibration

Figure 1 shows three examples of images captured from MAST shot no. 23344 by a Photron<sup>13</sup> Ultima APX-RS camera located at equatorial port 10. The images provide a view of the entire plasma, including the divertor region and strike points. The images are 8-bit grayscale and have a resolution of  $512 \times 528$  pixels. The projection properties of the optics, i.e., the line of sight of each pixel, must be known in order to use the image as a quantitative spatial measurement. Using a calibration procedure based on the visibility of the center column and the poloidal field coils and a simple camera model, the required parameters are estimated. In Appendix B the calibration procedure is elaborated. The resulting fit of the tokamak structures on the image is shown in Fig. 12(a).

During the discharge, significant horizontal movement of the tokamak center in the images is observed. To compensate this disturbance, the horizontal coordinate of the tokamak center is determined for each image so that the reconstructed plasma surface does not show this horizontal shift. Figure 12(b) shows the evolution of the tokamak center horizontal pixel coordinate  $x_0$  during discharge no. 23344. The horizon-

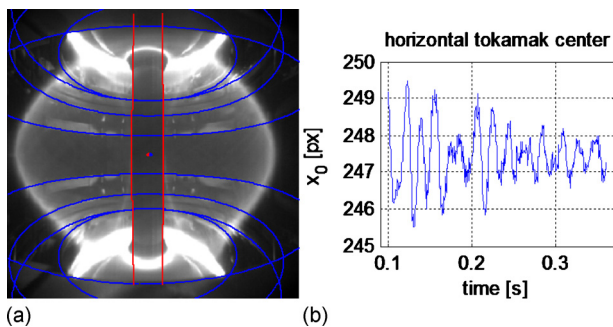


FIG. 12. (Color online) (a) Tokamak structures in image. (b) Tokamak center horizontal pixel coordinate during discharge.

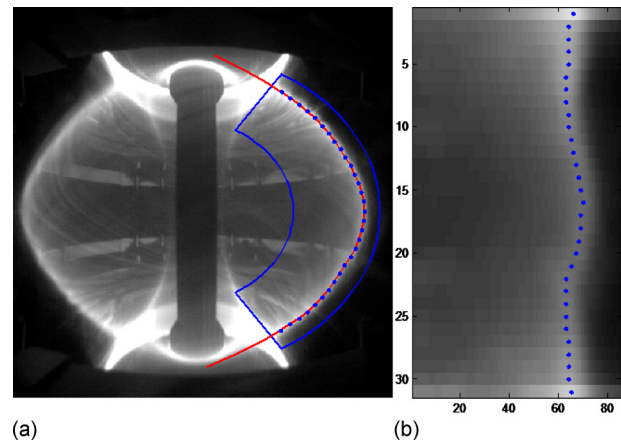


FIG. 13. (Color online) Detection of the right outer plasma edge, showing (a) region of interest, detected edge points, and piecewise polynomial fit. (b) Resampled and filtered pixel grid with maximum value pixels on each row marked.

tal tokamak center pixel coordinate  $x_0$  is then used to define the horizontal camera coordinate  $u_c$  to be used in the reconstruction equations. At a distance of  $w_c = 2.08$  m from the camera, a 1 pixel displacement in  $x_0$  corresponds to a change in  $u_c$  of 7 mm.

### B. Edge detection

The full view images of MAST shown in Fig. 1 can be treated as two poloidal view images in the left and right half of the image. In each of the two poloidal images, the plasma edge has the form of two lines; an inner and an outer plasma edge, intersecting at the top and bottom of the image in the case of a dual null divertor plasma. To locate the edges, regions of interest (ROIs) are appointed in the image having the shape of a curved rectangle around the expected plasma edges. In the ROIs, the image is resampled and filtered to form rectangular pixel grids. On each row of this grid, the maximum intensity is identified as the plasma edge. The degree of smoothing is optimized to reduce sensitivity to noise and filaments while maintaining resolving power. Adaptive ROIs can be used to cater for different phases of the discharge with significantly different plasma shapes. The detection of the outer plasma edge in the divertor regions is hampered by the presence of other, sharper edges in this part of the image and the low contrast of the plasma edge. Therefore, the ROI chosen for the outer edge is limited to the central part of the outer edge up to the intersection with the inner plasma edge. Figure 13 illustrates the detection of the outer plasma edge.

To improve the robustness of the detected edge, which may contain spurious edge points, a piecewise polynomial function is fitted through the edge coordinates, such that the effect of noise on individual edge points is reduced but the overall shape of the plasma edge is retained. The here applied fit is formed of a fourth order polynomial around the equatorial plane and two second order polynomials for the top and bottom of the edges, joined with continuous first derivative. The use of these functions also allows extrapola-

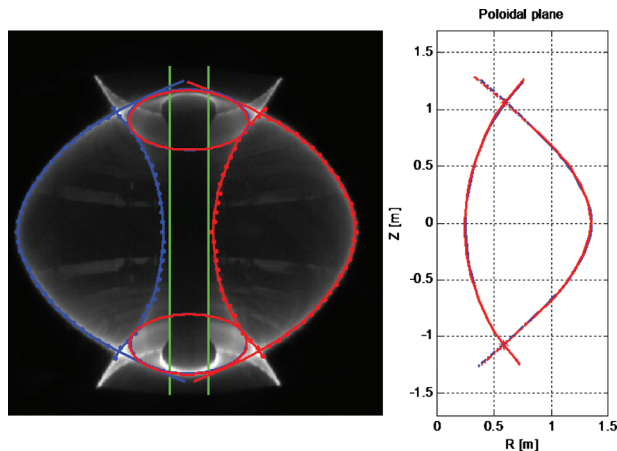


FIG. 14. (Color) Plasma shape reconstruction in MAST discharge no. 23344. Reconstructions from both the left (blue) and right (red) halves of the image are shown. Extrapolated plasma edges are shown as the dashed-dotted lines.

tion of the plasma edges in regions of the image where edge detection is problematic, such as the divertor region for the outer plasma edge.

During ELMs, such as shown in Fig. 1(c), large filaments show up and the plasma edge is less localized. The plasma edge can still be identified during an ELM but the noise and uncertainty are momentarily higher.

### C. Optical plasma shape reconstruction: OFIT

Given the two edges in the image and the projection properties of the camera, the edges are projected onto the projection surface  $(u, v)$  and plasma surface reconstruction is performed using the coordinate transform described in Sec. II A. This procedure is abbreviated as the OFIT reconstruction. Because of the toroidal symmetry of the plasma, the two halves of the image effectively provide two measurements of the plasma shape. However, as the camera is not pointed exactly at the tokamak center, the two half images are not symmetric. Only after reconstruction of the plasma shape from both half images will two similar plasma shapes be obtained. Figure 14 shows a camera image of a DND plasma from MAST discharge no. 23344 and the corresponding OFIT reconstruction from both halves of the image.

As described in Sec. II C, the inner and outer plasma edges span a different height after reconstruction. The outer plasma edge is defined only in a limited domain, approximately  $-0.8 < Z < 0.8$ , because of the limited visibility of the outer edge in the divertor region. To extend the outer plasma edge beyond this range, an extrapolation using the fitted piecewise polynomial functions is used, also shown in Fig. 14. This extrapolation allows making an estimate of the x-point locations of the DND plasma, as the outer plasma edge now intersects the inner plasma edge in the poloidal plane. However, this extrapolation introduces extra uncertainty and noise to the detected x-point locations.

During the initial phase of a discharge, the plasma is in limiter configuration before forming an upper and lower x-point. An x-point plasma can be optically recognized by its so called strikes: the legs that extend from the x-points out-

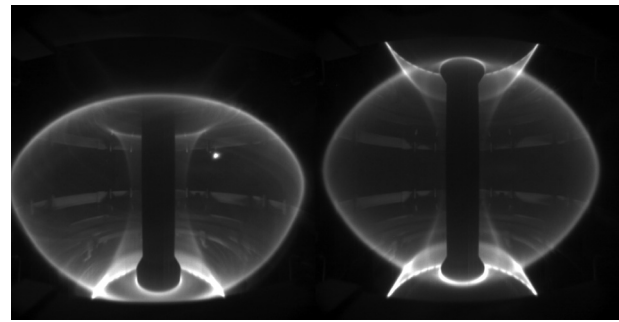


FIG. 15. Images of MAST H-mode plasmas in SND (left) and DND (right) configurations.

ward to the divertor targets. Figure 15 shows MAST plasmas in lower single null divertor (SND) and DND configurations. The distinct feature of the DND plasma in the top half of the image is the outer strike: the inner plasma edge extending beyond the outer edge toward the divertor. The top end of the SND plasma has the same qualitative shape as the circular plasma in Fig. 7(a). The transition from limiter to x-point configuration in the images, however, is not sharp. Figure 16 shows three images of the transition from limiter to x-point plasma in the first 0.1 s of MAST discharge no. 23344. As the magnetic topology evolves from limiter to x-point configuration, strikes gradually become visible. Because of the finite thickness of the emission layer, there is no discrete transition in the images between the limiter and the x-point configuration. Additionally, the emission of light is not as strongly concentrated on the LCFS in this early phase of the discharge, further amplifying this effect. Discriminating between x-point and limiter plasmas during this transition on the basis of the images is therefore a matter of choosing an arbitrary threshold.

Because OFIT does not yet cater for the reconstruction of limiter or SND plasmas, only the part of the discharge that is optically recognized as a DND plasma is reconstructed. In MAST discharge no. 23344, this holds for  $t > 0.1$  s.

Based on the toroidal symmetry of the plasma, comparing plasma shape reconstructions from the left and right halves of the image can provide insight into the effects of errors in camera calibration and uncertainties introduced in edge detection and reconstruction. To compare the two reconstructions, a set of 13 shape descriptors is used: the inner and outer plasma edge radii at  $Z=0.5$  and  $Z=-0.5$ , the minimum and maximum plasma radius, the  $R$  and  $Z$  coordinates of both x-points, the elongation  $\kappa$ , and the upper and lower triangularities  $\delta_{UP}$  and  $\delta_{LOW}$ .

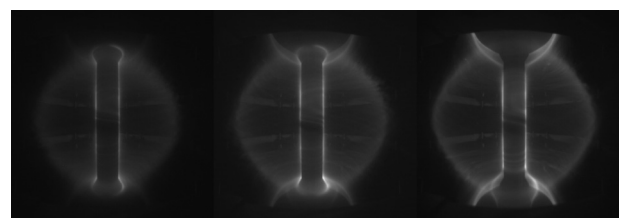


FIG. 16. Transition from limiter to x-point plasma during the first 0.1 s of MAST discharge no. 23344.

TABLE I. Deviations of shape descriptors between reconstructions from left and right half image.

	$\sigma_1$	$\sigma_2$
$R_{\min}$	4.6 mm	6 mm
$R_{x,\text{upper}}$	-1.9 mm	24 mm
$Z_{x,\text{upper}}$	-12 mm	27 mm
$R_{o,0.5}$	-2.0 mm	5.6 mm
$R_{i,0.5}$	6.1 mm	8.4 mm
$\delta_{\text{UP}}$	0.0097	0.044
$\kappa$	0.0022	0.033
$R_{\max}$	0.6 mm	4.8 mm
$R_{x,\text{lower}}$	1.5 mm	15 mm
$Z_{x,\text{lower}}$	-6.6 mm	19 mm
$R_{o,-0.5}$	-6.2 mm	5.0 mm
$R_{i,-0.5}$	1.4 mm	5.9 mm
$\delta_{\text{LOW}}$	0.0032	0.029

Two measures of errors are used for each set of signals  $s_1$  and  $s_2$  on the interval  $(t_1, t_2)$

$$\sigma_1 = \frac{\int_{t_1}^{t_2} s_1 - s_2 dt}{t_2 - t_1}, \quad (16)$$

$$\sigma_2 = \sqrt{\frac{\int_{t_1}^{t_2} (s_1 - s_2 - \sigma_1)^2 dt}{t_2 - t_1}}, \quad (17)$$

such that  $\sigma_1$  is a measure of average constant offset and  $\sigma_2$  is a measure of offset-corrected variance between the signals. The value of  $\sigma_2$  is treated as an uncertainty band. When, for a set of two signals,  $\sigma_1 > \sigma_2$ , there exists a significant constant offset. In comparing the left and right OFIT reconstructions, this may indicate errors in the camera calibration.

For each of the shape descriptors, the error measures between OFIT from both half images are given in Table I. For a selection of the shape descriptors, the signals from both optical reconstructions are also plotted in Fig. 17. The optical

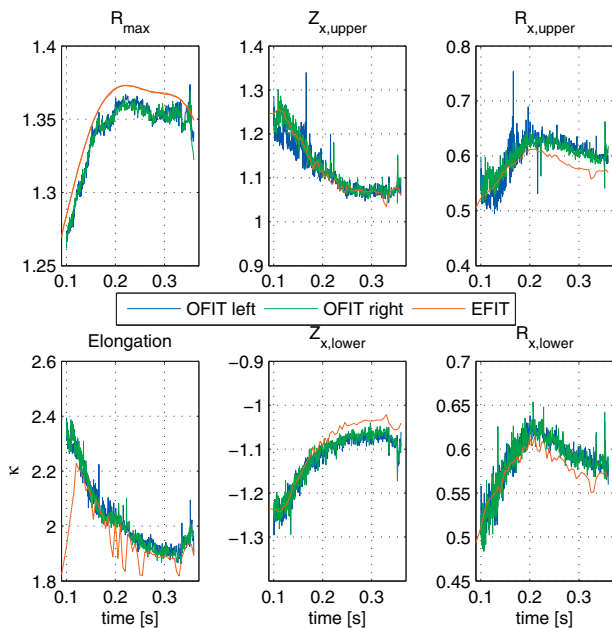


FIG. 17. (Color) Time traces of shape descriptors from OFIT and EFIT.

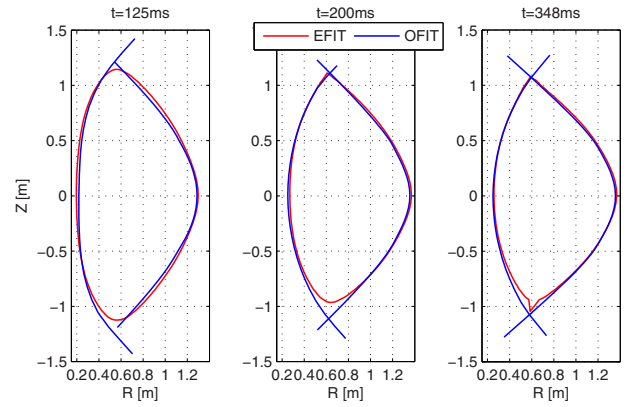


FIG. 18. (Color online) Plasma edge cross sections from EFIT and OFIT for three MAST shot no. 23344 equilibriums.

reconstructions show upper and lower triangularity  $\delta_{\text{UP}}$  and  $\delta_{\text{LOW}}$  of around 0.36 for most of the discharge. The definitions of elongation and triangularity of Beghi and Cenedese<sup>6</sup> are used.

For almost all of the 13 shape descriptors  $\sigma_2 > \sigma_1$ , indicating good agreement within the uncertainty band that is approximated by  $\sigma_2$ . Only the outer lower plasma radius  $R_{o,-0.5}$  shows an offset that is larger than the uncertainty band, indicating there may be a small error in the calibration parameters or a shortcoming in the camera model. Arguably, the tokamak construction tolerances may be such that the plasma is not exactly toroidally symmetric.

The effect of extrapolation of the outer plasma edges on the reconstructed x-point locations is obvious from the larger uncertainties present in these shape quantities. This uncertainty could be greatly reduced by placing additional cameras at approximately x-point height that provide a near-horizontal view of the plasma edge in the x-point region, resulting in a reconstruction of the x-points similar in accuracy to the  $R_{\max}$  signal from the equatorial camera.

## D. Comparison to EFIT reconstructions

Figure 18 shows EFIT and OFIT reconstructions of equilibriums from MAST shot no. 23344. Table II shows the error measures [Eqs. (16) and (17)] of the shape descriptors between EFIT and OFIT. In this case, the average of the OFIT

TABLE II. Deviations of shape descriptors between OFIT and EFIT.

	$\sigma_1$	$\sigma_2$
$R_{\min}$	-8.7 mm	14 mm
$R_{x,\text{upper}}$	17 mm	17 mm
$Z_{x,\text{upper}}$	-3.3 mm	18 mm
$R_{o,0.5}$	-14 mm	7.6 mm
$R_{i,0.5}$	-7.8 mm	12 mm
$\delta_{\text{UP}}$	-0.044	0.049
$\kappa$	0.064	0.082
$R_{\max}$	-14 mm	4.1 mm
$R_{x,\text{lower}}$	8.1 mm	14 mm
$Z_{x,\text{lower}}$	-19 mm	18 mm
$R_{o,-0.5}$	-9.2 mm	11 mm
$R_{i,-0.5}$	-19 mm	11 mm
$\delta_{\text{LOW}}$	-0.017	0.051

reconstructions from the left and right half images is used to compare to the EFIT reconstruction. A significant offset of 14 mm is present in the  $R_{\max}$  signal, also clearly visible in Fig. 17. An offset of similar magnitude is present in the  $R_{o,0.5}$  and  $R_{o,-0.5}$  signals. The EFIT reconstruction relies on optical constraints for the midplane outer plasma edge. This constraint is applied such that the LCFS at the outer edge is placed 1 cm outboard of the optically detected peak of Dalphi emission, partially explaining the  $R_{\max}$  offset.<sup>14</sup>

The EFIT reconstructions show a limiter plasma until  $t=0.125$  s before switching to a DND configuration, whereas the images and therefore OFIT show a DND plasma from before  $t=0.1$  s. EFIT does, however, detect x-points for  $t < 0.125$  s, albeit outside of the LCFS, whose locations agree well with those found by OFIT, as can be seen in Fig. 17. For  $t > 0.125$  s, the EFIT reconstruction alternates between a DND and SND plasma, where the lower x-point is sometimes placed just outside of the LCFS when it is located on a marginally different magnetic flux surface. These small excursions of the x-points over the flux surfaces are not apparent in the images and thus in the OFIT reconstructions.

The EFIT reconstructions show a triangularity of approximately  $\delta=0.4$  during most of the shot versus  $\delta=0.36$  for OFIT. The difference in triangularity between EFIT and OFIT results from the differences in x-point locations and  $R_{\max}$  signals. The optical reconstruction detects the x-points at a larger radius  $R$  but shows a smaller  $R_{\max}$ , resulting in a lower triangularity.

The elongation signals from EFIT and OFIT shown in Fig. 17 have a significant offset only between  $t=0.1$  s and  $t=0.125$  s. In this part of the discharge, EFIT detects a limiter configuration and places both x-points outside the LFCS, meaning the top and bottom extremes of the LCFS are closer and the resulting elongation is lower. The dips in the EFIT signal for  $t > 0.125$  s occur when a SND plasma is detected. The elongations found by OFIT are always based on the x-points of the plasma and agree to within 3% of the DND equilibria from EFIT.

#### IV. APPLICATIONS AND DISCUSSION

The agreement in shape and the correlation in time between the EFIT and OFIT plasma shape reconstructions suggest the magnetic and emissive properties of the plasma edge are closely related and the optical boundary reconstruction provides a measurement of the plasma boundary that is valid within the uncertainty bounds.

Visible accessibility of the plasma edge is required for the optical shape reconstruction. In many tokamaks, the vacuum vessel fits tightly around the plasma. The lens of the camera must then also be placed close to the plasma to have an unobscured view of the plasma. This camera location, however, means that only a fraction of the plasma edge is visible in the camera image, as explained in Sec. II A. To perform a reconstruction of the full plasma shape, multiple cameras will then be required, each viewing a part of the plasma circumference. The MAST tokamak is unique in this respect; its open design allowing a full view of the plasma using only a single camera.

To optimize the resolution and sensitivity of the reconstruction, a configuration with nearly horizontal sightlines is desired. The MAST images used in this paper are made using a wide angle lens viewing the top and bottom of the plasma at large angles to the horizontal plane. This setup limits the accuracy of the reconstruction around the x-points. Extra cameras at approximately x-point height can greatly improve the accuracy of the x-point localization. During some MAST discharges, a low framerate camera has been placed in the upper and lower ports, the so called DIVCAM. The resulting images provide a nearly horizontal view of the strikes and x-point. Preliminary results of boundary reconstructions using DIVCAM images suggest that the reconstruction of the outer strike from the midplane camera is accurate while the reconstruction of the inner strike, based on an extrapolation of the outer plasma edge, has a systematic offset of around 5 cm at the strike point.

The MAST images used in this paper are intensity maps of visible light; no optical wavelength filtering other than the camera's inherent sensitivity is applied. Using wavelength specific filters may provide clearer images and result in a more reliable reconstruction. Previous research on the DIII-D tokamak has shown distinct emission footprints around the LCFS for different characteristic wavelengths.<sup>15</sup>

#### A. OFIT for real-time control

In this case study, all processing is done in MATLAB functions. A single reconstruction of the plasma shape in MAST, including image processing and centering, curve fitting, coordinate transform, and x-point detection takes 3 ms on a desktop computer with an Intel Core 2 6600 central processing unit. Using both halves of the image to effectively obtain two reconstructions takes 4.5–5 ms.

Real-time optical detection of the plasma midplane outer radius for feedback control is already routinely applied at MAST with a cycle time of 0.5 ms. An implementation of the optical shape reconstruction in a real-time environment such as currently used in MAST (Ref. 16) can provide a real-time diagnostic usable for feedback control. Currently available real-time cameras and frame grabbers can provide several thousand full resolution frames per second.<sup>15,17</sup> The cycle time of this diagnostic would therefore depend strongly on the processing power of the applied system. The 3 ms processing time of the shape reconstruction implemented in MATLAB can be seen as the minimum achievable speed for the real-time diagnostic.

As tokamaks grow, both PF-coil inductive time constants and plasma skin times lengthen, effectively lowering the sampling requirements for a real-time diagnostic. A real-time control application of OFIT therefore is expected to be feasible in the near future.

To operate OFIT in a control loop of plasma position and shape, the behavior of the diagnostic must be known in all plasma regimes and the quality of the boundary reconstruction must be sufficient. Different plasmas of various shapes, densities, confinement modes, and turbulence levels will result in very different images and will often require modifications to the image processing and the camera shutter timing to optimally identify the plasma edge. The different images

obtained in different plasma regimes can result in a varying accuracy of the reconstructed plasma shape. For example, a high density H-mode discharge will produce a bright image with very sharp plasma edges and is very well suited for optical boundary reconstruction. On the other hand, an L-mode plasma with strong turbulence will show a much fuzzier image and will result in a more uncertain boundary reconstruction. The diagnostic is required to detect and adapt to different plasma regimes and to not only provide a plasma shape but also an indication of the current regime and the corresponding reliability of the boundary reconstruction.

For this research, OFIT was developed to explore the possibilities of optical plasma boundary reconstruction and was tuned to a small number of MAST DND discharges. More work is needed to obtain a plasma shape diagnostic that is flexible, robust, and automatically adapts to different plasma regimes.

## B. OFIT as a scientific diagnostic

Currently, only indirect (magnetic) or local (MAST linear HOMER camera,<sup>16</sup> plasma boundary reflectometry,<sup>18</sup> or Thomson scattering<sup>19</sup>) boundary diagnostics are available in tokamak operation. OFIT uniquely provides a direct and independent measurement of the entire plasma boundary.

Different plasma boundary diagnostics measure different physical properties of the plasma. Magnetic reconstructions generally provide the plasma boundary as the last closed (poloidal-) flux surface. Reflectometry provides the location of an arbitrary density surface. Thomson scattering provides local electron density and temperature profiles. OFIT reconstructs the boundary from the light emitted from the vicinity of the plasma boundary.

To relate these measurements, a detailed model of the plasma boundary is required. However, the availability of those measurements also aids in developing such a plasma edge model. Ultimately, given enough understanding of the details of plasma edge physics, different boundary diagnostics are equivalent. In this case, a strong argument for installing the required cameras for OFIT boundary reconstruction is the simplicity and independence of the diagnostic that can potentially reconstruct the entire plasma boundary. OFIT can then provide a strong, global constraint to equilibrium reconstruction codes such as EFIT and diagnostics such as motional Stark effect arrays.

## V. CONCLUSIONS

An optical plasma shape diagnostic, OFIT, is developed and applied to images of MAST discharges. Comparison of the optically reconstructed plasma shapes with reconstructions available from EFIT show spatial agreement within 19 mm and strong temporal correlation. The processing time for a single MAST plasma shape reconstruction in its current MATLAB implementation is 3 ms and scales with processing power of the applied system. The speed of the algorithm allows application in real-time environments such as feedback control of the plasma shape. Further development is needed, however, to obtain the desired robustness and accuracy in all plasma regimes. Specifically, a robust and adap-

tive edge detection procedure is required to interpret the images from plasmas in different phases of the discharge and with different emission regimes. Some plasmas may not provide enough edge localization to reach the accuracy required for control of the plasma boundary.

An important prerequisite for the new diagnostic is the optical accessibility to the plasma edge. Multiple cameras will be required in tokamaks with tight fitting vacuum vessels, where a single camera cannot view all of the plasma circumference. In open tokamaks such as MAST, applying multiple cameras placed at different heights will also result in a more accurate and reliable reconstruction by providing a more horizontal view of the plasma edges far from the mid-plane. The use of divertor cameras in MAST to obtain better x-point and strike-point localization is currently being explored.

Having detected in the image the shape of the plasma edge, other visible features such as filaments and hot spots can also be detected and their orientation can be related to the local plasma edge. A single diagnostic can then provide information about plasma shape, PFC loads, and ELM activity with low relative error, paving the way to intelligent sensing and integrated control of the plasma edge.

The coordinate transform derived for the optical plasma shape reconstruction can find applications in various analysis tools for line of sight measurements by providing the location of the plasma edge in the coordinates of the diagnostic and is already being used at MAST.

## ACKNOWLEDGMENTS

This work, supported by NWO and the European Communities under the contract of the Association EURATOM/FOM, was carried out within the framework of the European Fusion Programme. The views and opinions expressed herein do not necessarily reflect those of the European Commission. The authors would like to thank Nicola Bertelli, Michel van Hinsberg, and the colleagues at the TU/e DCT-lab for fruitful discussions and support. Equipe Tore Supra is kindly acknowledged for making Fig. 8 available.

## APPENDIX A: SYSTEM OF A CIRCULAR PLASMA IMAGE

The newly derived coordinate transform is mathematically validated for a circular tokamak plasma. To do so, a poloidal view image of a circular plasma is synthesized using a different approach to the coordinate transform. Again, it is assumed that sightlines tangent to the plasma surface will result in edge points in the image.

A point on the circular plasma surface and the normal vector  $V_n$  to this surface are expressed in Cartesian coordinates  $(u, v, w)$  in terms of the toroidal and poloidal angles  $\varphi$  and  $\theta$

$$\begin{bmatrix} u_t \\ v_t \\ w_t \end{bmatrix} = \begin{bmatrix} \cos(\phi)[r \cos(\theta) + R_0] \\ r \sin(\theta) \\ \sin(\phi)[r \cos(\theta) + R_0] \end{bmatrix},$$

$$V_n = \begin{bmatrix} \cos(\phi)\cos(\theta) \\ \sin(\theta) \\ \sin(\phi)\cos(\theta) \end{bmatrix}.$$

The sightline vector from a camera at  $(u_c, v_c, w_c)$  is

$$V_l = \begin{bmatrix} u_t - u_c \\ v_t - v_c \\ w_t - w_c \end{bmatrix} = \begin{bmatrix} \cos(\phi)[r \cos(\theta) + R_0] - u_c \\ r \sin(\theta) - v_c \\ \sin(\phi)[r \cos(\theta) + R_0] - w_c \end{bmatrix}.$$

For the sightline to be tangent to the plasma surface, the dot product of the surface normal and the sightline vectors must equal 0.

$$V_n \cdot V_l = 0.$$

This allows, for a given poloidal angle  $\theta$ , to find the toroidal angle  $\phi$  of the tangent point on the plasma surface. Solving for  $\phi$  results in

$$u_c \cos(\phi) + w_c \sin(\phi) = R_0 + \frac{r - v_c \sin(\theta)}{\cos(\theta)},$$

which can be further simplified to

$$\sqrt{u_c^2 + w_c^2} \sin \left[ \phi + \arctan \left( \frac{u_c}{w_c} \right) \right] = R_0 + \frac{r - v_c \sin(\theta)}{\cos(\theta)}.$$

Substituting into the right-hand-side of Eq. (10), the  $R$ ,  $Z$ , and  $dR/dZ$  coordinates of a circular plasma

$$R = R_0 + r \cos(\theta),$$

$$Z = r \sin(\theta),$$

$$\frac{dR}{dZ} = -\tan(\theta),$$

result in the same equation. The coordinate transform is therefore validated for the special case of a circular plasma.

Given the poloidal angle  $\theta$  the tangent point can now be found. The projection of this point is obtained by drawing a line from the camera through the tangent point and taking the intersection of this line with the projection surface.

## APPENDIX B: CAMERA CALIBRATION

To use the camera images as a quantitative measurement, the projection properties of the optics, i.e., the line of sight of each pixel, must be known. A model of the camera projection is presented and the parameters are estimated using a calibration procedure based on the visibility of the center column and the poloidal field coils and on the knowledge of the charge coupled device (CCD) dimensions and the focal length of the lens. The result will be the projection function

$$(u, v) = f_p(x, y),$$

where  $x$  and  $y$  are pixel coordinates in the image and  $u$  and  $v$  are coordinates on the  $(u, v)$  projection plane.

The pinhole camera model with its optical axis normal to the  $(u, v)$  projection plane is used, providing an affine scaling from pixel coordinates to projection plane. A first order barreling correction accounts for lens distortion. The required camera parameters are then the camera location  $(u_c, v_c, w_c)$ ,

TABLE III. Camera calibration parameters.

$w_c$	2.08 m
$x_{oc}$	252 px
$y_{oc}$	276.5 px
$K_B$	$4 \times 10^{-4}$
$l_p$	17 $\mu$ m
$f$	5 mm
$y_0$	276.5 px

the barreling factor  $K_B$ , the scaling factor  $K_{scale}$ , and the location of the optical center in the image  $(x_{oc}, y_{oc})$ .

The barreling correction assumes a first order barreling model<sup>20</sup> of the form

$$x_{bc} - x_{oc} = (x - x_{oc})[1 + K_b \sqrt{(x - x_{oc})^2 + (y - y_{oc})^2}],$$

$$y_{bc} - y_{oc} = (y - y_{oc})[1 + K_b \sqrt{(x - x_{oc})^2 + (y - y_{oc})^2}],$$

where  $(x, y)$  is the pixel coordinate in the image and  $(x_{bc}, y_{bc})$  is the barreling-corrected pixel coordinate, corresponding to the image taken with an ideal linear lens.

With the camera's optical axis parallel to the  $w$ -axis, the projection coordinates  $(u, v)$  are then calculated from the barreling-corrected pixel coordinates  $(x_{bc}, y_{bc})$  by the projection functions

$$u - u_c = w_c K_{scale,x} (x_{bc} - x_{oc}),$$

$$v - v_c = w_c K_{scale,y} (y_{bc} - y_{oc}).$$

The camera coordinates  $u_c$  and  $v_c$  are derived from the location of the tokamak center in the image  $(x_0, y_0)$  using the same equations

$$u_c = -w_c K_{scale,x} (x_0 - x_{oc}),$$

$$v_c = -w_c K_{scale,y} (y_0 - y_{oc}).$$

The vertical tokamak center coordinate  $y_0$  is fixed while the horizontal coordinate  $x_0$  is updated for every frame based on the location of the inner plasma edges.

Given the focal distance of the applied lens and the dimensions of the pixels on the CCD chip, the scaling factor  $K_{scale}$  can be determined as

$$K_{scale} = \frac{l_p}{f},$$

where  $l_p$  is the size of a pixel on the CCD and  $f$  is the focal length of the lens. It is assumed that the CCD is at a distance  $f$  from the lens.

The calibration parameters used to draw the PF-coil edges in Fig. 12(a) are given in Table III, where  $l_p$  and  $f$  are camera specifications and the other parameters are tuned manually to obtain the best fit of the coil edges on the image.

<sup>1</sup>H. Weisen, Y. Martin, J.-M. Moret, and the TCV Team, *Nucl. Fusion* **42**, L5 (2002).

<sup>2</sup>J.-M. Moret M. Anton, S. Barry, R. Behn, G. Besson, F. Biihlmann, A. Burri, R. Chavan, M. Corboz, C. Deschenaux, M. J. Dutch, B. P. Duval, D. Fasel, A. Favre, S. Franke, A. Hirt, F. Hofmann, C. Hollenstein, P.-F. Isoz, B. Joye, J. B. Lister, X. Llobet, J. X. Magnin, P. Mandrin, B. Marletaz, P. Marmillod, Y. Martin, J.-M. Mayor, J. Moravec, C. Nieswand, P. J. Paris, A. Perez, Z. A. Pietrzyk, V. Piffil, R. A. Pitts, A. Pochelon, O. Sauter, W. van Toledo, G. Tonetti, M. Q. Tran, F. Troyon, D. J. Ward, and

- H. Weisen, *Plasma Phys. Controlled Fusion* **37**, A215 (1995).
- <sup>3</sup>F. Crisanti, P. J. Lomas, O. Tudisco, A. B'ecoulet, M. B'ecoulet, L. Bertalot, T. Bolzonella, G. Bracco, M. De Benedetti, B. Esposito, C. Giroud, N. C. Hawkes, T. C. Hender, O. N. Jarvis, E. Joffrin, D. Pacella, V. Riccardo, F. Rimini, K. D. Zastrow, and contributors to the EFDA-JET Work Programme, *Plasma Phys. Controlled Fusion* **45**, 379 (2003).
- <sup>4</sup>W. Suttrop, O. Gruber, B. Kurzan, H. D. Murmann, J. Neuhauser, J. Schweinzer, J. Stober, W. Treutterer, and the ASDEX Upgrade Team, *Plasma Phys. Controlled Fusion* **42**, A97 (2000).
- <sup>5</sup>J. Luo, *Plasma Sci. Technol.* **4**, 1183 (2002).
- <sup>6</sup>A. Beghi and A. Cenedese, *IEEE Control Syst. Mag.* **25**, 44 (2005).
- <sup>7</sup>Ph. Moreau, F. Saint-Laurent, and J. B. Lister, *Fusion Eng. Des.* **84**, 1339 (2009).
- <sup>8</sup>R. Albanese, G. Artaserse, M. Mattei, O. Tudisco, and JET-EFDA Contributors, *Int. J. Appl. Electromagn. Mech.* **26**, 191 (2007).
- <sup>9</sup>A. Kirk, N. Ben Ayed, G. Counsell, B. Dudson, T. Eich, A. Herrmann, B. Koch, R. Martin, A. Meakins, S. Saarelma, R. Scannell, S. Tallents, M. Walsh, H. R. Wilson, and the MAST Team, *Plasma Phys. Controlled Fusion* **48**, B433 (2006).
- <sup>10</sup>D. P. Kostomarov, A. A. Lukianitsa, F. S. Zaitsev, R. J. Akers, L. C. Appel, D. Taylor, and V. V. Zlobin, *Proceedings of the 32nd EPS Conference on Plasma Physics*, Tarragona, Spain, 27 June–1 July 2005 (ECA, 2005), Vol. 29C, p. 1.092.
- <sup>11</sup>See <http://www.fusion.org.uk/mast/index.html> for Mega-Ampere Spherical Tokamak.
- <sup>12</sup>See <http://www-fusion-magnetique.cea.fr/gb/cea/ts/ts.htm> for Tore Supra tokamak.
- <sup>13</sup>See <http://www.photron.com/> for Photron high-speed cameras.
- <sup>14</sup>J. Storrs (private communication).
- <sup>15</sup>M. Groth, M. E. Fenstermacher, G. D. Porter, R. L. Boivin, N. H. Brooks, W. P. West, P. C. Stangeby, and D. G. Whyte, presented at the Proceedings of the 44th Annual Meeting Division of Plasma Physics, Orlando, FL, 11–15 November 2002.
- <sup>16</sup>J. Storrs, J. Dowling, G. Counsell, and G. McArdle, *Fusion Eng. Des.* **81**, 1841 (2006).
- <sup>17</sup>See <http://www.visionresearch.com/> for Vision Research high speed cameras.
- <sup>18</sup>C. E. Kessel and N. L. Bretz, *Nucl. Fusion* **39**, 445 (1999).
- <sup>19</sup>H. Murmann and M. Huang, *Plasma Phys. Controlled Fusion* **27**, 103 (1985).
- <sup>20</sup>D. C. Brown, *Photogramm. Eng.* **7**, 444 (1966).